Effect of flow-field structure on discharging and charging behaviors of hydrogen/bromine redox flow batteries

Kyeongmin Oh[a], Michael C. Tucker[b], Adam Z. Weber[b], and Hyunchul Ju[a,*]

[a]Department of Mechanical Engineering

Inha University

100 Inha-ro, Nam-Gu, Incheon 402-751, Republic of Korea

and

[b]Environmental Energy Technologies Division

Lawrence Berkeley National Laboratory

Berkeley, CA, USA

A manuscript submitted to

Electrochimica Acta

as a technical paper

[*]Corresponding author. E-mail: hcju@inha.ac.kr, ph: +82-32-860-7312, fax: +82-32-868-1716

ABSTRACT

Designing and optimizing the flow-field structure for the liquid phase Br_2/HBr electrolyte solution of H_2/Br_2 redox flow batteries (RFBs) is important for improving cell performance. In this study, two electrolyte flow modes, i.e. the flow-by and flow-through modes, are simulated by using a three-dimensional H_2/Br_2 RFB model. The model is first applied to real-scale H_2/Br_2 cell geometries and then validated against the experimental polarization curves acquired using the two different flow modes. The model predictions compare well with the experimental data and further highlight the advantages of using the flow-through mode relative to the flow-by mode. Detailed multi-dimensional contours of the electrolyte flow velocity and key species distributions reveal that more uniform diffusion and stronger convective transport are achieved by using the flow-through mode, which alleviates the ohmic loss associated with charge transport in the Br_2 electrode.

KEYWORDS: Hydrogen bromine redox flow batteries; Numerical simulation; Flow mode; Convection; Bromide

1. INTRODUCTION

With the growing importance of grid-scale energy storage, the hydrogen/bromine redox flow battery (RFB) has received much attention due to its superior regenerative behavior and lower electrolyte cost. Recently, a high power density of 1.4 $W \cdot cm^{-2}$ and slow degradation of the RFB performance over 10,000 h were reported for 10−25 cm^2 lab-scale cells [1–5]. As shown in **Fig. 1**, in the hydrogen/bromine RFB system, gaseous hydrogen and an aqueous solution of bromine (Br_2) and hydrobromide (HBr) are fed into the negative and positive electrodes, respectively. These two electrodes are separated by a thin proton exchange membrane (PEM) such as DuPont's Nafion®. Several design issues related to sealing and manifolding may arise, particularly when the cell is scaled up to larger sizes and stacks for grid-level energy storage. Flow-field design and optimization become more critical in facilitating the distribution of reactants and removing products in large-scale cells.

Cho et al. [6] evaluated two different flow-field configurations (flow-by and flow-through modes) for supply of aqueous Br_2/HBr to cells with an active area of 10 cm^2. In the flow-by mode, the aqueous Br_2/HBr mixture is first fed into the flow channels and then diffuses toward the reaction site in the porous electrode, whereas the Br_2/HBr electrolyte directly penetrates through the porous electrode in the flow-through mode. Roughly, 23% improvement in the maximum power density was reported by using the flow-through mode instead of the flow-by mode. The enhanced performance achieved with the former was attributed to the stronger convective electrolyte flow in the Br_2 electrode driven by the flow-through mode, leading to enhanced removal of the discharge product (HBr) from the cell, thereby minimizing

membrane dehydration and proton resistance. Those results clearly illustrated the substantial impact of the flow-field design on the performance of H_2/Br_2 RFBs.

To scale up the lab-scale cell (a few cm^2) to a practical large-scale cell for grid-level energy storage applications (from several hundreds to thousands of cm^2), three-dimensional (3-D) modeling and real-scale simulations are required to fully elucidate the complex electrochemical and transport phenomena occurring in the real-scale cells. This understanding is key to successful design and operation of H_2/Br_2 RFB systems. In this study, a three-dimensional, transient H_2/Br_2 RFB model developed in a previous study [7] is applied to a real-scale cell with an active area of 10 cm^2. In order to reduce the computational turnaround time involved in a large numerical mesh with millions of grid points, the 3-D H_2/Br_2 RFB code is parallelized for parallel computing. Emphasis is placed on exploring the effects of the electrolyte flow mode in the Br_2 electrode (i.e. flow-by vs. flow-through mode) on the multi-dimensional reactant and product distributions, and the resultant voltage loss and cell performance. Such an elaborate simulation tool for the prediction of electrochemical performance and transport phenomena is highly desirable in the design and engineering of large-scale H_2/Br_2 RFBs.

2. NUMERICAL MODEL

2.1. Model assumptions

The 3-D H_2/Br_2 RFB model developed previously [7] accounts for the redox reactions of H_2 and Br_2/HBr solutions and the resulting species transport inside the cell. The assumptions made in the model are as follows:

1) Gaseous or aqueous flow is incompressible and laminar because of the low flow velocity.
2) The porous electrodes are characterized by effective porosity and permeability.
3) The cell is assumed to be isothermal during charge and discharge.
4) The gas mixtures obey the idea gas law due to low pressure.
5) The gravitational effect is neglected.
6) The dilute solution theory is employed to describe species transport.

2.2. Conservation equations and source terms

Based on the assumptions above, the present H_2/Br_2 RFB utilizes four principles of conservation: mass, momentum, species, and charge. The mass and momentum conservation equations are given as follows:

Mass conservation: $$\frac{\partial \varepsilon \rho}{\partial t} + \nabla \cdot \left(\rho \vec{u} \right) = 0 \tag{1}$$

Momentum conservation: $$\frac{1}{\varepsilon}\left[\frac{\partial \rho \vec{u}}{\partial t} + \frac{1}{\varepsilon} \nabla \cdot \left(\rho \vec{u} \vec{u} \right) \right] = -\nabla P + \nabla \cdot \tau + \rho \vec{g} - \frac{\mu}{K} \vec{u} \tag{2}$$

where ε denotes the porosity of the porous components of the H_2/Br_2 cell and superficial velocities are used to automatically ensure mass flux continuity at the interface between the porous and non-porous regions inside the cell (e.g. the interfacial surface between the diffusion layer and channel).

In the H_2 electrode, the gas phase is assumed to be dominant. Therefore, ρ for the hydrogen side of Eqs. (1) and (2) is the gas mixture density, which varies according to the molar concentrations of the gases based on the ideal gas law. On the other hand, the aqueous Br_2/HBr solution prevails in the Br_2 electrode, and thus the total liquid mixture density is used for the bromine side:

$$\rho = \begin{cases} \sum_i C_i M_i & (\mathrm{H_2\ electrode}) \\ \sum_i \rho_i \cdot vf_i = \sum_i c_i \cdot M_i & (\mathrm{Br_2\ eletrode}) \end{cases} \tag{3}$$

In Eq. (2), K is the effective permeability of the porous component, which is determined by the Kozeny–Carman equation:

$$K = \frac{4r_{PM}^2}{C_{KC}} \frac{\varepsilon^3}{\left(1-\varepsilon\right)^2} \tag{4}$$

The species conservation equations can be derived by individual species balance analyses that entail a detailed account of the species consumption/production by electrochemical reactions, as well as species transport through the cell components by various modes.

$$\frac{\partial\left(\varepsilon C_i\right)}{\partial t} + \nabla \cdot \vec{N}_i = S_i \tag{5}$$

Here, $\vec{N}_i$ accounts for the flux of each species via diffusion, migration, convection, and electro-osmosis and can be described as follows:

$$\vec{N}_i = \underbrace{\left(-D_i^{eff} \nabla C_i\right)}_{Diffusion} + \underbrace{\left(-\frac{z_i F}{RT} D_i^{eff} C_i \nabla \phi_e\right)}_{Migration} + \underbrace{C_i \vec{u}}_{Convection} + \underbrace{\frac{n_{d,i}}{F} \vec{i}_e}_{Electro-osmosis} \tag{6}$$

In the diffusion term, D_i^{eff}, represents the effective diffusion coefficient of species i through various cell components. For the porous components, D_i^{eff} should be modified

from its intrinsic value by using the Bruggeman correlation [8] to account for the effects of porosity and tortuosity as follows:

$$D_i^{eff} = \varepsilon^r D_i \tag{7}$$

The electro-osmotic drag (EOD) coefficient, $n_{d,i}$, in the electro-osmosis term is only relevant to the water and bromine species, and thus its value for hydrogen gas is set to zero.

The charge transport due to the electrochemical reactions is governed by the principle of charge conservation:

$$\nabla \cdot \vec{i}_e = \nabla \cdot \vec{i}_s = S_\phi \tag{8}$$

where $\vec{i}_e$ and $\vec{i}_s$ denote the ionic and electronic current densities throughout the cell components, respectively. The values are given by:

$$\vec{i}_e = \sum_i \vec{i}_i = -\kappa^{eff} \nabla \phi_e - F \sum_i z_i \left(D_i^{eff} \nabla C_i + C_i \vec{u} \right)$$

(9)

$$\vec{i}_s = \sigma^{eff} \nabla \phi_s \tag{10}$$

In the above equations, the effective ionic conductivity, κ^{eff}, and the effective electronic conductivity, σ^{eff}, are defined for the various components of the H_2/Br_2 cell.

$$\kappa^{eff} = \begin{cases} \varepsilon_{hCL}^{ionomer} \kappa_{mem} & \text{for } H_2 \text{ electrode} \\ \kappa_{mem} & \text{for membrane} \\ F^2 \sum_i z_i^2 D_i^{eff} C_i / RT & \text{for } Br_2 \text{ electrode} \end{cases} \tag{11}$$

$$\sigma^{eff} = \begin{cases} (1-\varepsilon)^r \sigma & \text{for porous layers} \\ \sigma_{FFP} & \text{for flow-field plates} \end{cases} \tag{12}$$

For κ_{mem} in Eq. (11), the ionic conductivity data measured by Kusoglu et al. [9] was interpolated as a function of the bromide concentration, C_{Br^-}, and used for the simulations in order to predict the effect of membrane dehydration via bromide during H_2/Br_2 RFB operation.

$$\kappa_{mem} = 7.749 + \left(-\frac{3.171}{1.328\sqrt{\pi/2}} \right) \exp\left[-2\left(\frac{C_{Br^-} - 1.317}{1.328} \right)^2 \right] \quad \text{for } 0 \le C_{Br^-} < 3.3M \qquad (13)$$

The source terms of the aforementioned conservation equations are identified for the various components of the H_2/Br_2 cell and are summarized in **Table 1**.

2.3. Electrochemical reactions

During discharge, H_2 and Br_2 are fed into the cell and H_2 is then oxidized to protons (H^+) while Br_2 is reduced to bromide (Br^-). The reverse reactions occur during the charge process.

Br_2 electrode: $Br_2(aq) + 2e^- + 2H^+ \underset{\text{charge}}{\overset{\text{discharge}}{\rightleftharpoons}} 2HBr(aq) \quad E_{0,b} = 1.09\text{V}$ (23)

H_2 electrode: $H_2(g) \underset{\text{charge}}{\overset{\text{discharge}}{\rightleftharpoons}} 2H^+(aq) + 2e^- \quad E_{0,h} = 0.00\text{V}$ (24)

Overall: $H_2(g) + Br_2(\text{aq}) \underset{\text{charge}}{\overset{\text{discharge}}{\rightleftharpoons}} 2HBr \quad E_{0,eq} = 1.09\text{V}$ (25)

Here, E_0 represents the standard equilibrium potential and the subscript zero signifies the standard state conditions, which can be calculated from the thermodynamic properties under standard state conditions.

The volumetric transfer current density, *j*, for the above half-reactions in Eqs. (23) and (24) can be obtained from the general Butler–Volmer equations as follows:

Br_2 electrode: $j_b = a_b i_{0,b} \left[\frac{C^s_{Br^-}}{C^{ref}_{Br^-}} \exp\left(\frac{\alpha_{a,b} F}{RT} \eta_b \right) - \frac{C^s_{Br_2}}{C^{ref}_{Br_2}} \exp\left(-\frac{\alpha_{c,b} F}{RT} \eta_b \right) \right]$ (26)

$$\text{H}_2 \text{ electrode: } j_h = a_h i_{0,h} \left(\frac{C_{H_2}}{C_{H_2}^{ref}} \right)^{\frac{1}{2}} \left[\exp\left(\frac{\alpha_{a,h} F}{RT} \eta_h \right) - \exp\left(-\frac{\alpha_{c,h} F}{RT} \eta_h \right) \right] \tag{27}$$

where *a* and α denote the electrochemically active surface area per unit of electrode volume and the transfer coefficients of the redox reactions, respectively. The surface concentration of species *i* (*i* denotes either Br^- or Br_2), C_i^s, can be calculated from the local consumption or production of species *i* by the redox reactions:

$$FD_{Br^-} \frac{C_{Br^-}^{bulk} - C_{Br^-}^{s}}{r_{PM}} = i_{0,b} \left[\frac{C_{Br^-}^{s}}{C_{Br^-}^{ref}} \exp\left(\frac{\alpha_{a,b} F}{RT} \eta_b \right) - \frac{C_{Br_2}^{s}}{C_{Br_2}^{ref}} \exp\left(\frac{-\alpha_{c,b} F}{RT} \eta_b \right) \right] \tag{28}$$

$$2FD_{Br_2} \frac{C_{Br_2}^{bulk} - C_{Br_2}^{s}}{r_{PM}} = i_{0,b} \left[\frac{C_{Br_2}^{s}}{C_{Br_2}^{ref}} \exp\left(\frac{-\alpha_{c,b} F}{RT} \eta_b \right) - \frac{C_{Br^-}^{s}}{C_{Br^-}^{ref}} \exp\left(\frac{\alpha_{a,b} F}{RT} \eta_b \right) \right] \tag{29}$$

The surface overpotentials of the redox half-reactions in Eqs. (23) and (24) are defined as follows:

$$\text{Br}_2 \text{ electrode: } \eta_b = \phi_s - \phi_e - E_{eq} \tag{30}$$

$$\text{H}_2 \text{ electrode: } \eta_h = \phi_s - \phi_e \tag{31}$$

where ϕ_s and ϕ_e denote the electronic and electrolyte potentials, respectively, at the phase interface of each electrode. In Eq. (30), E_{eq}, representing the equilibrium potential of the H_2/Br_2 cell, can be obtained from the Nernst equation as follows:

$$E_{eq} = 1.2679 - 0.0006105T + \frac{RT}{2F} \ln\left(\frac{C_{Br_2} \cdot C_{H_2}}{C_{HBr}^2} \right) \tag{32}$$

Therefore, it is evident that the surface overpotentials in Eqs. (30) and (31) are relative to that of the standard hydrogen electrode.

2.4. Bromine species crossover model

The crossover of bromine species through the membrane may cause several critical issues in terms of the cell performance and durability, including self-discharge, coulombic losses, membrane dehydration, platinum poisoning on the H_2 side, etc. Therefore, accurate modeling of the bromine/bromide crossover phenomena is required in order to authentically capture the charge and discharge behaviors of the H_2/Br_2 cell. Typically, the Br_2 electrode is fed with concentrated bromide solutions ($C_{Br^-} > C_{Br_2}$) in order to decrease crossover of bromine species through the membrane. Under these conditions, Br_2 favorably interacts with Br^- to form tri-bromide (Br_3^-); thus, the concentration of Br_2 in the solution phase can be deduced to be very small compared to that of Br_3^-. Based on Eq. (6), the crossover fluxes of bromine species (Br_2, Br^-) through the membrane are expressed as:

$$\vec{N}_{Br^-}^{xover} = -D_{Br^-}^{eff} \nabla C_{Br^-}^{*} - \frac{z_{Br^-} F}{RT} D_{Br^-}^{eff} C_{Br^-}^{*} \nabla \phi_e \qquad \text{for } Br^- \tag{33}$$

$$\vec{N}_{Br_2}^{xover} = -D_{Br_3^-}^{eff} \nabla C_{Br_3^-} + \frac{n_{d,Br/H^+}}{F} \vec{i} \qquad \text{for } Br_2 \tag{34}$$

In the above equations, the contribution of convection to the overall crossover is neglected because the permeability of the membrane is very low, and thus the fluid velocity approaches zero in the membrane. More importantly, it should be noted that the diffusion term in the bromine crossover equation, Eq. (34), is expressed in terms of the concentration of tri-bromide, $C_{Br_3^-}$, because most of the Br_2 is complexed as Br_3^- in the solution at the equilibrium between the bromine species, and hence Br_3^- rather than Br_2 diffuses through the membrane. The second term on the right-hand side of Eq. (34) represents bromine species transport via electro-osmosis, wherein $n_{d,Br/H^+}$ is the electro-osmotic drag (EOD) coefficient, which is defined as the number

of bromine molecules dragged by each proton through the membrane (C_{Br}/C_{H^+}). $n_{d,Br/H^+}$ can be further expressed in terms of the EOD coefficient of water, $n_{d,H_2O/H^+}$, which has been well documented in the literature.

$$n_{d,Br/H^+} = n_{d,H_2O/H^+}\frac{C_{Br}}{C_{H_2O}} \tag{35}$$

Tucker et al. [10] measured the crossover fluxes of water and bromine species under various state-of-charge (SOC) and charge current density conditions. Using the crossover data, the crossover diffusivity of tri-bromide, $D^{eff}_{Br_3^-}$, in Eq. (34) was estimated and used for the simulations. The estimated value was 3.7×10^{-11} $m^2 \cdot s^{-1}$, which falls well within the range of values reported in the literature (approximately 10^{-12} to 10^{-10} $m^2 \cdot s^{-1}$) [10, 11].

2.5. Boundary conditions and numerical implementations

The 3-D H_2/Br_2 RFB model described in the previous section is applied to a cell with a geometry consisting of the membrane, catalyst layer (CL), porous electrode, and flow field plate (FFP). The kinetic, physiochemical, and transport properties are summarized in **Table 2**. **Figure 2** shows the detailed cell geometries and mesh configurations of the real-scale experimental H_2/Br_2 cells evaluated by Cho et al. [6], where the aqueous Br_2/HBr electrolyte was fed through two different flow-field structures corresponding to the flow-by and flow-through modes. In the flow-by mode, a single serpentine flow field was used to distribute the Br_2/HBr electrolyte over the electrode. To access the reaction sites, the electrolyte is transported through the bromine porous medium (bPM), mainly via diffusion. On the other hand, the aqueous Br_2/HBr electrolyte is directly forced to flow through the bPM in the flow-through mode. Detailed cell dimensions and initial/boundary conditions for the H_2/Br_2

RFB simulations are listed in **Table 3**. No-slip and impermeable velocity conditions are applied to the external surfaces of the computational domain, except for the inlets and outlets, for the momentum equations. As indicated in **Fig. 2**, the inlet velocities, v_{in}, for the hydrogen gas can be expressed as functions of the stoichiometric ratio, operating current density, cross-sectional area of the gas channel, and the hydrogen concentration (which is a function of the inlet pressure and temperature). On the other hand, the Br_2/HBr solution streams can be determined from the volumetric flow rate (driven by the pump) and the cross-sectional area of the channel.

$$v_{in,h} = \xi_h \frac{i}{2F} \frac{1}{C_{H_2}} \frac{A_{act}}{A_{in,h}} \tag{36}$$

$$v_{in,b} = \frac{Q_b}{A_{in,b}} \tag{37}$$

During charge and discharge, the H_2/Br_2 cell is operated in either the galvanostatic or potentiostatic mode. Therefore, while the electric potential, Φ_s, of the outer wall of the FFP in the hydrogen side is fixed, either constant cell voltage or constant current density can be applied to the outer side wall of the bFFP.

$$\begin{aligned} &\mathrm{H_2\ FFP\ (x=0)} \quad \phi_s = 0 \\ &\mathrm{Br_2\ FFP\ (x=L_x)} \begin{cases} \phi_s = V_{cell} & \text{for potentiostatic mode} \\ \sigma^{eff} \nabla \phi_s = \vec{i}_{cell} & \text{for galvanostatic mode} \end{cases} \end{aligned} \tag{38}$$

In Eq. (38), $\vec{i}_{cell}$ denotes the current applied to the cell. The other external surfaces, including the top, bottom, front, and rear surfaces of the computational domain, are assumed to be electrically insulated.

The 3-D H_2/Br_2 RFB model comprising the aforementioned governing equations and source terms was implemented in the commercial fluid dynamics (CFD) software program, Fluent, by using user-defined functions (UDFs). The convergence criteria were set to 10^{-8} for the equation residuals. According to our grid-independent

test, the computational cells shown in **Fig. 2** require around one million grid points, and thus a parallel computing technique was used to reduce the computational turnaround time. In general, a steady state H_2/Br_2 RFB simulation requires about 1000 iterations for maximum residuals of species equations less than 10^{-8} and takes nearly three hours using eight processors with 3.07 GHz CPUs (Intel® zeon) each with 48 GB memory (DDR3-1333).

3. RESULTS AND DISCUSSION

The H_2/Br_2 RFB model presented in the previous chapter was applied to the real-scale cell geometry and full 3-D simulations were carried out to investigate the effects of the Br_2/HBr electrolyte flow mode (i.e. flow-by vs. flow-through mode). **Figure 3** shows a comparison of the simulation results and the experimental data measured by Cho et al. [6] at various discharge current densities. With good agreement between the simulation and experiment, both clearly demonstrate that the flow-through mode is advantageous at intermediate and high current densities. Therefore, it is evident that the flow mode design of the H_2/Br_2 RFB has a substantial influence on ohmic and mass-transfer losses.

The Br_2 profiles in the cross-sections cutting through the middle of the cell (y = 16 mm) and the end of cell (y = 30 mm) at the discharge current density of 0.9 $A \cdot cm^{-2}$ are plotted in **Fig. 4**. During discharge, Br_2 is reduced to HBr by the half-cell reaction described by Eq. (23) and thus the Br_2 concentration continues to decrease in moving downstream in both flow modes. The cross-sectional Br_2 profiles along y = 16 mm and 30 mm are similar in the case of the flow-through mode, where the minimum Br_2 concentrations in the middle and end planes are slightly different, i.e. 826 and 830 $mol \cdot m^{-3}$, respectively. Unlike the flow-through mode, different Br_2 profiles are observed in the case of the flow-by mode. More severe Br_2 depletion occurs in the middle plane (y = 16 mm), where the minimum Br_2 concentration is relatively low (around 779 $mol \cdot m^{-3}$). In contrast, Br_2 depletion is greatly mitigated in the end plane (y = 30 mm), leading to a relatively higher minimum Br_2 concentration (i.e. 843 $mol \cdot m^{-3}$). This trend is mainly due to the difference in the degree of convective transport of Br_2 between the two planes in the flow-by configuration. The end plane (y = 30 mm) is located close to the underside of the U-turn regions, and thus strong

convective flow is induced, which promotes overall Br_2 transport within the electrode. On the other hand, Br_2 in the middle plane is transported via diffusion only, resulting in a significant concentration gradient along the electrode thickness.

Figure 5 displays the HBr profiles in the same cross-sections cutting through the middle and end of the cell for the same two cases (the flow-by and flow-through modes at 0.9 $A \cdot cm^{-2}$). In the flow-through mode, the rate of HBr removal is similar in the middle and end planes, clearly indicative of a similar convective effect in both planes. In contrast, for the flow-by mode, efficient removal of HBr was achieved in the end plane (y = 30 mm) owing to the stronger convective effect underneath the U-turn regions, whereas the degree of HBr accumulation is relatively high in the middle plane (y = 16 mm) due to the weaker convective transport there. Comparison of the Br_2 and HBr profiles (**Figs. 4 and 5**) clearly indicates that the flow-through mode induces uniform convective flow within the bPM, facilitating more uniform reactant supply (Br_2) and product removal (HBr).

Figure 6 presents the velocity distributions over the middle plane of the bPM for the two flow modes. For the flow-by mode, relatively higher velocities are observed underneath the U-turn regions. The velocities in the bPM underneath the U-turn region (red dashed box) and the other straight channel region (blue dashed box) are approximately 0.1389 and 0.0463 $m \cdot s^{-1}$, respectively, where the velocity is roughly three times larger near the U-turn regions. Therefore, the increased convective transport near the U-turn regions helps to improve the mass transport of Br_2 and HBr and results in smaller concentration gradients within the bPM underneath the U-turn regions, which is consistent with the Br_2 and HBr concentration profiles shown in **Figs. 4 and 5**. In contrast, a more uniform velocity profile in the bPM was predicted with the flow-through mode, where the average velocities in the blue and

red dashed bPM regions are similar in magnitude (0.0696 vs. 0.0708 $m \cdot s^{-1}$) and are nearly unidirectional from the inlet toward the outlet along the z direction. As indicated in **Fig. 6**, the average velocities in the bPM for the flow-through and flow-by modes are 0.0668 $m \cdot s^{-1}$ and 0.0435 $m \cdot s^{-1}$, respectively, indicating that the overall strength of convective flow in the bPM is larger in the flow-through mode compared to the flow-by mode.

The current density distributions over the membrane at the discharge current density of 0.9 $A \cdot cm^{-2}$ are shown in **Fig. 7a**. Owing to the high flow rates of the hydrogen and Br_2 reactants, the current density distribution along the flow-direction is quite uniform for both flow modes. On the other hand, the local current density gradient between the channel and rib regions is relatively larger in the flow-by mode than that in the flow-through mode, indicating that the local current density is mainly affected by Br_2 depletion under the ribs in the flow-by mode. Consequently, a high degree of uniformity in the current density distributions was achieved with the flow-through mode. The trend in the current density fluctuation between the channel and rib regions can be more clearly seen in **Fig. 7b**. For the flow-by mode, the local current density near the channel region is higher than that in the rib region, indicating that the current density is mainly determined by Br_2 transport. In contrast, higher current density is observed under the ribs for the flow-through mode, illustrating highly effective hydrogen transport and that electron transport through the hydrogen side is the main factor influencing the current density distribution.

The voltage losses for the respective flow modes are presented in **Fig. 8**, wherein the ohmic losses due to ionic charge transport through the hCL, bPM, and membrane, and the kinetic loss due to the Br_2 reduction reaction are plotted for comparative purposes. It is clear that the ohmic loss due to ionic charge transport

through the bPM is a major causative factor for the difference in performance between the two flow modes. Based on Eqs. (9) and (11), the ionic charge transport resistance through the bPM is determined by the effective diffusivities of the charged species, i.e. tri-bromide (Br_3^-) and protons (H^+), as well as the concentrations and velocities of these ions. During cell clamping, compression of the bPM in the flow-by design is concentrated in the region of the bPM in contact with the ribs of the bipolar plates, whereas in the flow-through design, the bPM is more uniformly compressed, leading to a lower degree of bPM compression. As a result, the effective diffusivities of Br_3^- and H^+ in the bPM are relatively lower and non-uniform in the flow-by mode, compared to those in the flow-through mode. The detailed properties of the compressed and uncompressed bPM are listed in **Table 2**. Besides the effective diffusivities of the ions, the convective transport of Br_3^- and H^+ in the bPM also affects the ohmic loss through the bPM. As seen in **Fig. 6**, the larger velocity in the bPM induced by the flow-through mode enhances the transport of Br_3^- and H^+, thus reducing the ionic charge transport resistance through the bPM.

Figure 9 shows a comparison of the calculated polarization curves for the two different flow modes during charge. A lower charge voltage was achieved with the flow-through cell configuration, which indicates that the convective flow inside the bPM enhanced by the flow-through mode results in superior mass and charge transport of Br_3^- and H^+ during charge. The breakdown of the charge voltages into individual voltage losses is also included in **Fig. 9**. Similar to the discharge processes, the ohmic loss through the Br_2 electrode is a significant contributor to the difference in performance between the flow-through and flow-by modes during the charge process.

The effect of bromine species crossover is expected to be important during the charge process because both the electro-osmotic and diffusive flux of bromine species across the membrane occur in the same direction from the Br_2 to the H_2 electrodes. The average diffusive, electro-osmotic, and total crossover rates of the bromine species through the membrane are plotted in **Fig. 10**. While the diffusion flux of the bromine species is almost invariant with increasing current density, the crossover of the bromine species due to electro-osmosis increases in proportion to the charge current density (see Eq. (6)). As a result, the overall crossover rate of bromine species through the membrane increases steeply with increasing charge current density. The substantial contribution of the electro-osmotic flux to the overall crossover flux results in an increase of the concentration of HBr in the hCL with charge current density. Regarding the effect of the bromine flow mode, the bromine crossover and HBr concentration curves were almost identical for the two flow modes, indicating that the impact of the bromine flow mode on the crossover of bromine species through the membrane is negligible.

4. CONCLUSION

The main focus of this study is to investigate the effects of the Br_2/HBr electrolyte flow modes (flow-by vs. flow-through mode) on the performance of RFBs. First, the 3-D H_2/Br_2 RFB model was applied to real-scale RFB geometries with different flow modes and then validated against the experimental polarization curves acquired during discharge. The superior cell performance achieved with the flow-through mode was successfully captured by the present model. The detailed simulation results clearly indicate that the ohmic loss due to charge transport via tri-bromide and protons in the bPM was substantially reduced by using the flow-through mode. This is due to more uniform and lower compression of the bPM in the flow-through hardware during cell assembly, compared to that in the flow-by hardware. Consequently, the flow-through mode led to higher effective diffusivities of Br_3^- and H^+ in the bPM and induced stronger convective flow of the Br_2/HBr electrolyte. These two factors are the main contributors to the reduced ionic charge transport resistance through the bPM in the flow-through configuration, leading to more uniform current density distribution and improved cell performance. This study illustrates that obtaining uniform electrolyte flow distributions inside the bPM is crucial for optimizing the cell performance, and the present 3-D computational model is a useful cell design tool for proper control of the electrolyte flow, particularly in large-scale H_2/Br_2 cells for grid-scale energy storage application.

ACKNOWLEDGEMENT

Nomenclature

A	cross-sectional area, m^2
a	specific surface area, m^{-1}
C	molar concentration, $mol \cdot m^{-3}$
C_{KC}	Kozeny-Carman constant
D	diffusion coefficient, $m^2 \cdot s^{-1}$
E_0	thermodynamic equilibrium potential, V
F	Faraday's constant, 96485 $C \cdot mol^{-1}$
i	current density, $A \cdot m^{-2}$
j	transfer current density, $A \cdot m^{-3}$
K	permeability, m^2
M	molecular weight, $kg \cdot mol^{-1}$
$\vec{N}$	species flux, $mol \cdot m^{-3} \cdot s^{-1}$
n_d	electro-osmotic drag coefficient
P	pressure, Pa
Q	volumetric flow rate, $m^3 \cdot s^{-1}$
R	universal gas constant, 8.314 $J \cdot mol^{-1} \cdot K^{-1}$
r_{PM}	pore radius in porous media, m
S	source/sink term
T	temperature, K
u	velocity, $m \cdot s^{-1}$
V_{cell}	cell voltage, V
vf_i	volume fraction of species i
z	valence

Greek symbols

α	transfer coefficient
ε	porosity
η	overpotential, V
κ	proton conductivity, $S \cdot m^{-1}$
μ	viscosity, $kg \cdot m^{-1} \cdot s^{-1}$
ρ	density, $kg \cdot m^{-3}$
σ	electronic conductivity, $S \cdot m^{-1}$
τ	viscous shear stress, $N \cdot m^{-2}$ or tortuosity
ϕ	potential, V

Subscript

0	equilibrium or initial value
a	anodic reaction value
b	bromine electrode side
c	cathodic reaction value
e	electrolyte
eq	equilibrium state
FFP	flow field plate
h	hydrogen electrode side
hCL	hydrogen catalyst layer
$\underline{i}$	species *i*
in	inlet
mem	membrane
s	solid (electronic)

u	momentum

Superscript

*	remain
bulk	bulk value
eff	effective
g	gas state
s	surface value
xover	crossover

References

[1] M.C. Tucker, K.T. Cho, A.Z. Weber, G. Lin, T.V. Nguyen, “Optimization of electrode characteristics for the Br_2/H_2 redox flow cell,” J. Appl. Electrochem. 45 (2015), 11-19.

[2] K.T. Cho, P. Albertus, V. Battaglia, A. Kojic, V. Srinivasan, A.Z. Weber, “Optimization and analysis of high-power hydrogen/bromine-flow batteries for grid-scale energy storage,” Energy Technol. 1 (2013), 596-608.

[3] G.G. Barna, S.N. Frank, T.H. Teherani, L.D. Weedon, “Lifetime studies in H_2/Br_2 fuel cells,” J. Electrochem. Soc. 131 (1984), 1973-1980.

[4] K.T. Cho, M.C. Tucker, M. Ding, P. Ridgway, V.S. Battaglia, V. Srinivasan, A.Z. Weber, “Cyclic performance analysis of hydrogen/bromine flow batteries for grid-scale energy storage,” ChemPlusChem 80 (2015), 402-411.

[5] G. Lin, P.Y. Chong, V. Yarlagadda, T.V. Nguyen, R.J. Wycisk, P.N. Pintauro, M. Bates, S. Mukerjee, M.C. Tucker, A.Z. Weber, “Advanced hydrogen-bromine flow batteries with improved efficiency, durability and cost,” J. Electrochem. Soc. 163 (2016), A5049-A5056.

[6] K.T. Cho, P. Ridgway, A.Z. Weber, S. Haussener, V. Battaglia, V. Srinivasan, “High performance hydrogen/bromine redox flow battery for grid-scale energy storage,” J. Electrochem. Soc. 159 (2012), A1806-1815.

[7] K. Oh, A.Z. Weber, H. Ju, “Three-dimensional modeling of H_2/Br_2 redox flow batteries,” Int. J. Hydrogen Energy, submitted.

[8] R.E. Meredith, C.W. Tobias In: Tobias CW, editor. “Advances in electrochemistry and electrochemical engineering,” vol. 2. New York: Interscience Publishers; 1962.

[9] A. Kusoglu, K.T. Cho, R.A. Prato, A.Z. Weber, “Structural and transport

properties of Nafion in hydrobromic-acid solutions," Solid State Ionics 252 (2013), 68-74.

[10] M.C. Tucker, K.T. Cho, F.B. Spingler, A.Z. Weber, G. Lin, "Impact of membrane characteristics on the performance and cycling of the Br_2-H_2 flow cell," J. Power Sources 284 (2015), 212-221.

[11] J.W. Park, R.Wycisk, P.N. Pintauro, "Nafion/PVDF nanofiber composite membranes for regenerative hydrogen/bromine fuel cells," J. Membrane Sci. 490 (2015), 103-112.

[12] F. Will, "Bromine diffusion through Nafion perfluorinated ion exchange membranes," J. Electrochem. Soc. 126 (1979), 36-43.

[13] B. Huskinson, M.J. Aziz, "Performance model of a regenerative hydrogen bromine fuel cell for grid-scale energy storage," Energy Science and Technology 5 (2013), 1-16.

[14] P. Chiaapr, H. Ju, "Three-dimensional non-isothermal modeling of a phosphoric acid-doped polybenzimidazole (PBI) membrane fuel cell," Solid State Ionics 225 (2012), 30-39.

[15] H. Al-Fetlawi, A.A. Shah, F.C. Walsh, "Non-isothermal modelling of the all-vanadium redox flow battery," Electrochimica Acta 55 (2009), 78-89.

[16] K.W. Knehr, E. Agar, C.R. Dennison, A.R. Kalidindi, E.C. Kumbur, "A transient vanadium flow battery model incorporating vanadium crossover and water transport through the membrane," J. Electrochem. Soc. 159 (2012), A1446-1459.

Table 1. Source/sink terms for H_2/Br_2 RFB model

Term	hCL			bPM		
Species conservation (S_i)	H_2	$-\frac{j_h}{2F}$	(14)	Br_2	$\frac{j_b}{2F}$	(15)
				Br^-	$-\frac{j_b}{F}$	(16)
Charge conservation (S_ϕ)	ϕ_e	j_h	(17)	ϕ_e	j_b	(18)
	ϕ_s	$-j_h$	(19)	ϕ_s	$-j_b$	(20)
Electro-chemical reactions ($\sum s_i M_i^z = ne^-$)	$H_2 - 2H^+ = 2e^-$		(21)	$2HBr - Br_2 - 2H^+ = 2e^-$		(22)

Table 2. Kinetic, physiochemical, and transport properties for H_2/Br_2 RFB model

Description		Value	Ref.
Exchange current density x ratio of reaction surface to electrode volume, *aj*	hCL	1.25×10^{8} $A\cdot m^{-3}$	[6]
	bPM	43,589.744 $A\cdot m^{-3}$	[6]
Porosity, ε	hPM	0.8	[6]
	hCL	0.3	[6]
	bPM	0.8 (uncompressed) 0.6 (compressed)	[6]
Ionomer volume fraction, $\varepsilon_{hCL}^{ionomer}$	hCL	0.64	[6]
Permeability, *K*	hPM	1.0×10^{-12} m^2	[14]
	hCL	1.0×10^{-13} m^2	[14]
	Membrane	1.0×10^{-18} m^2	[15][b]
Specific area, *a*	hCL	1.0×10^{5} m^{-1}	[a]
	bPM	4.0×10^{4} m^{-1}	[a]
Anodic/cathodic transfer coefficient, α	hCL	1.0/1.0	
	bPM	1.0/1.0	
Br_2 diffusivity, D_{Br_2}	PM, CL	1.42×10^{-9} $m^2\cdot s^{-1}$	[13]
	Membrane	3.702×10^{-11} $m^2\cdot s^{-1}$	[10][a]
Br^- diffusivity, D_{Br^-}	PM, CL	1.78×10^{-9} $m^2\cdot s^{-1}$	[13]
	Membrane	1.0×10^{-20} $m^2\cdot s^{-1}$	[b]
Electronic conductivity, σ	FFP	14,000 $S\cdot m^{-1}$	[14]
	PM	500 $S\cdot m^{-1}$	[14]
	CL	300 $S\cdot m^{-1}$	[14]
Pore radius of electrode, r_{PM}	bPM	50.3 μm	[16]
Kozeny-Carman constant, C_{KC}	bPM	5.55	[15]

[a]calculated, [b]assumed

Table 3. Cell dimensions and operating conditions

Description	Value	
Cell Dimensions		
Membrane thickness	50	μm
bPM thickness	780	μm
hCL thickness	8	μm
hPM thickness	235	μm
FFP thickness	2.0	mm
Channel height	1.0	mm
Channel/rib width	1.0	mm
Active area	10	cm^2
Operating conditions		
Stoichiometry for H_2 electrode	3.0	(100% H_2)
Inlet pressure in H_2 electrode	1.0	atm
Inlet Br_2 concentration during discharge/charge	900/232.5	$mol \cdot m^{-3}$
Inlet HBr concentration during discharge/charge	990/2325	$mol \cdot m^{-3}$
Volumetric flow rate in Br_2 electrode	100	$mL \cdot min^{-1}$
Inlet temperature	293.15	K

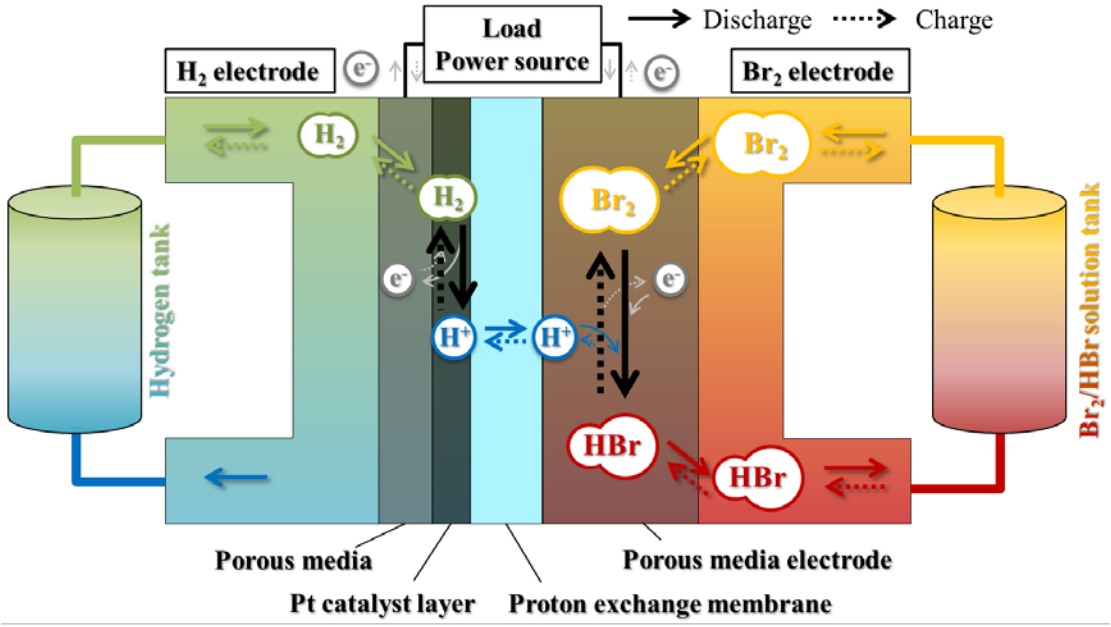

Fig. 1. Schematic diagram of hydrogen bromine redox flow battery.

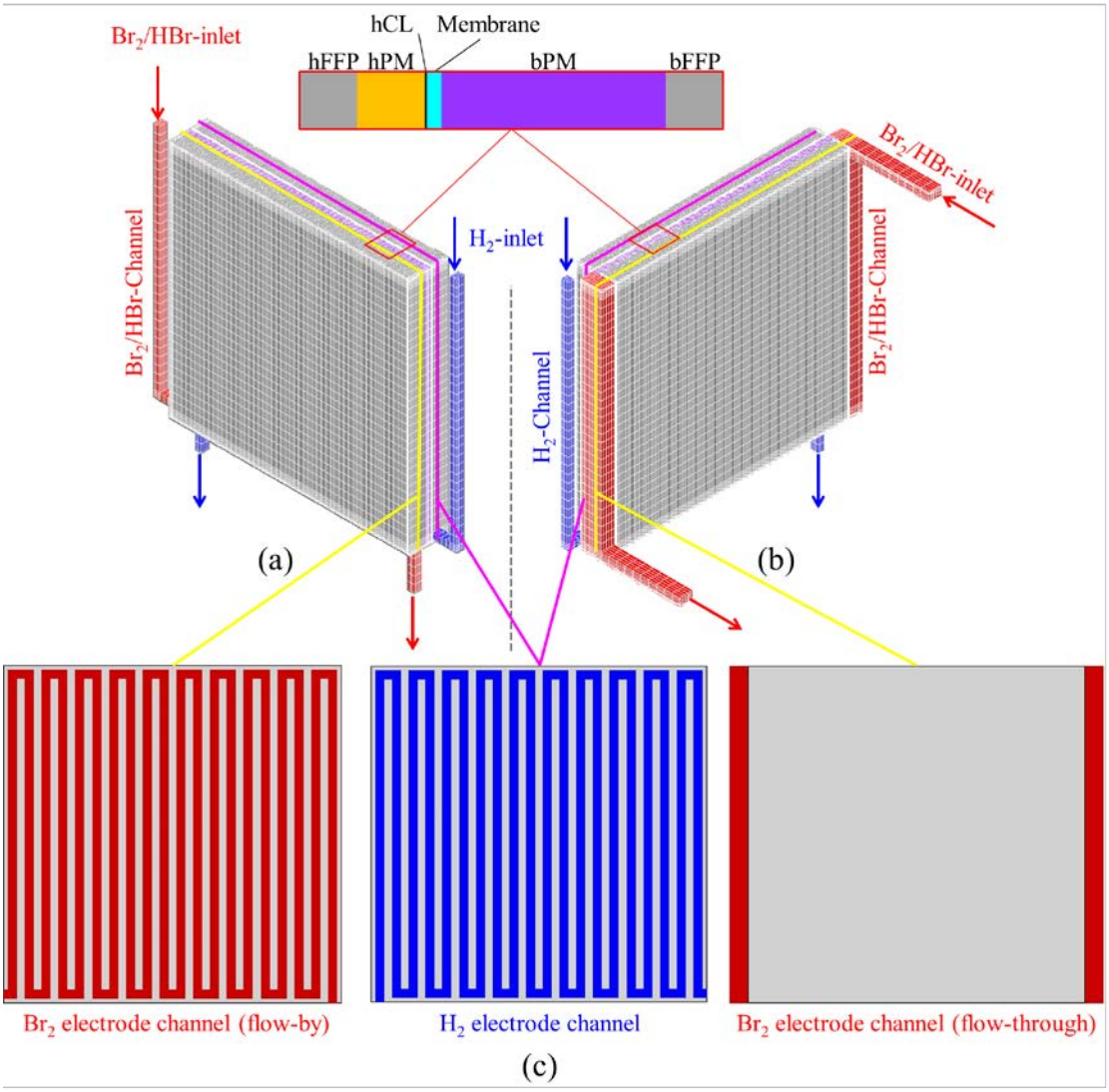

Fig. 2. Computational domain and mesh configuration of real scale H_2/Br_2 cells for (a) flow-by mode and (b) flow-through mode, which have (c) the cross-sectional shape of channels in H_2 and Br_2 electrode.

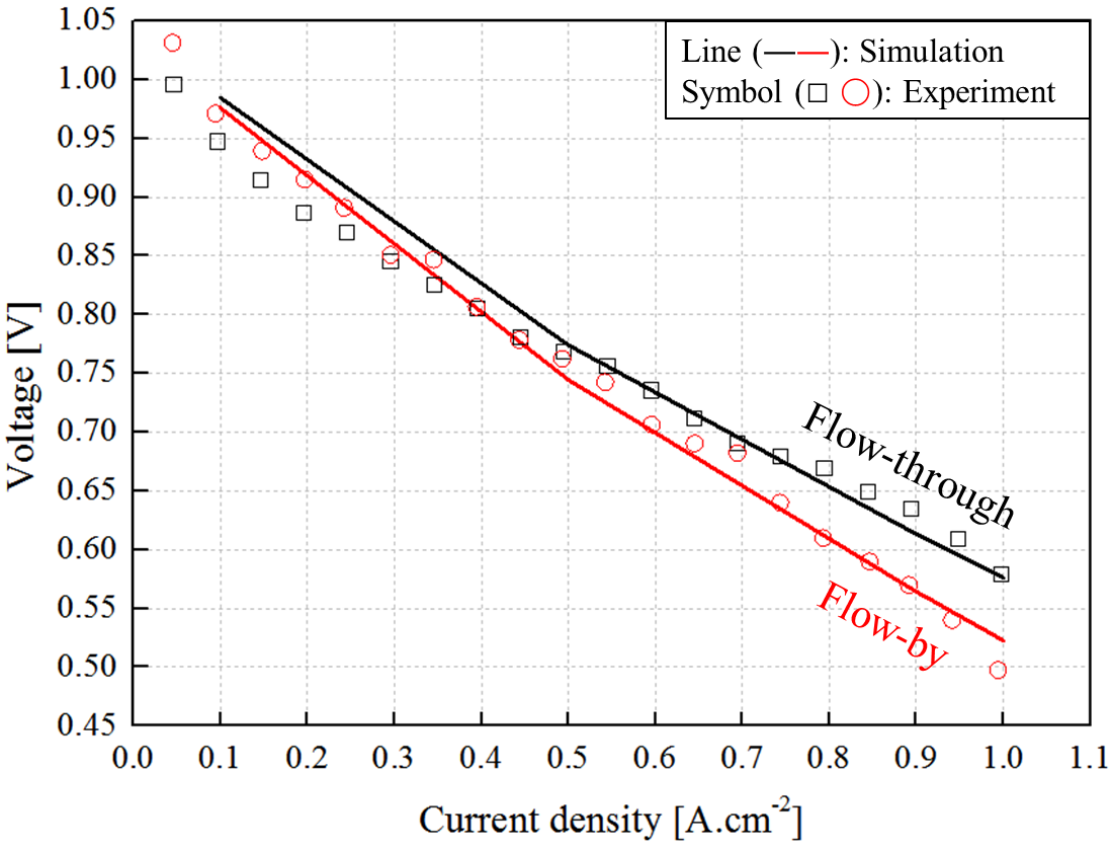

Fig. 3. Comparison of simulated (line) and measured (symbol) polarization curves during discharge for the flow-by and flow-through modes.

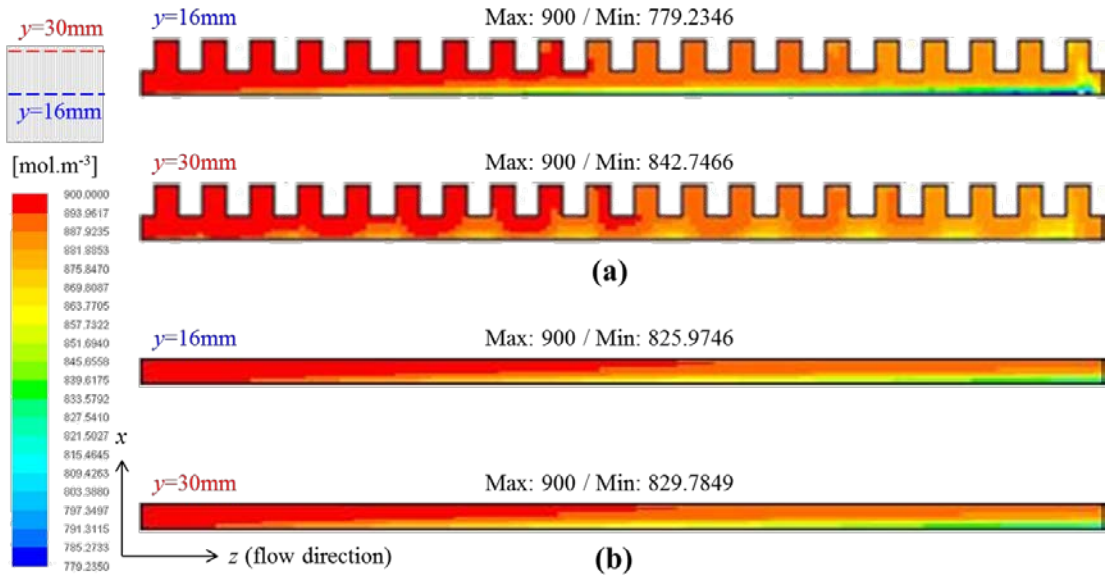

Fig. 4. Cross-sectional Br_2 concentration contours across the cell middle (y=16mm) and cell end (y=30mm) during discharge at 0.9A/cm^2 for (a) flow-bu mode and (b) flow-through mode.

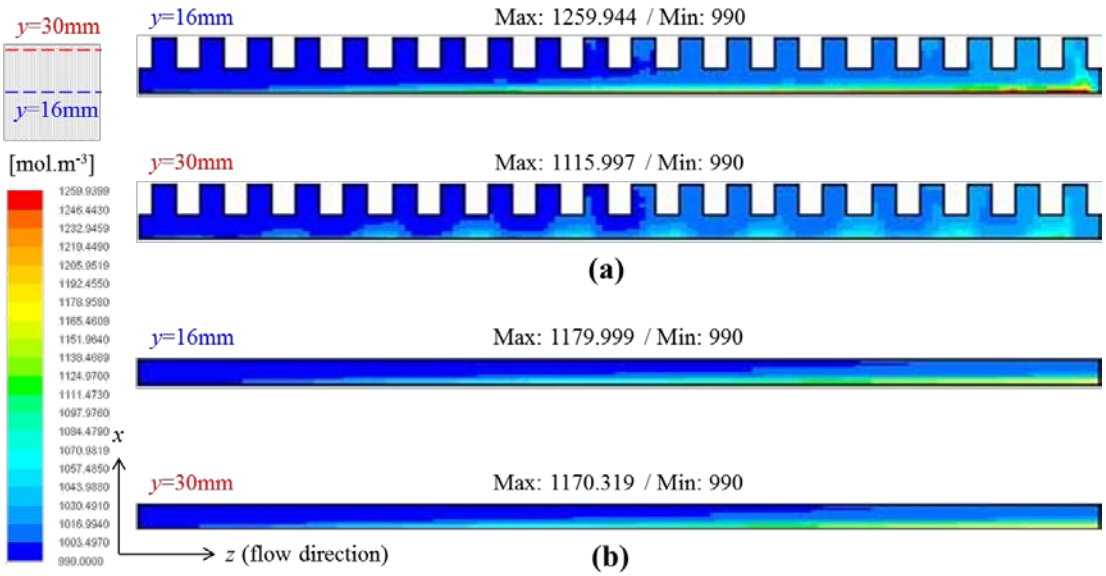

Fig. 5. Cross-sectional HBr concentration contours across the cell middle (y=16mm) and cell end (y=30mm) during discharge at 0.9A/cm^2 for (a) flow-by mode and (b) flow-through mode.

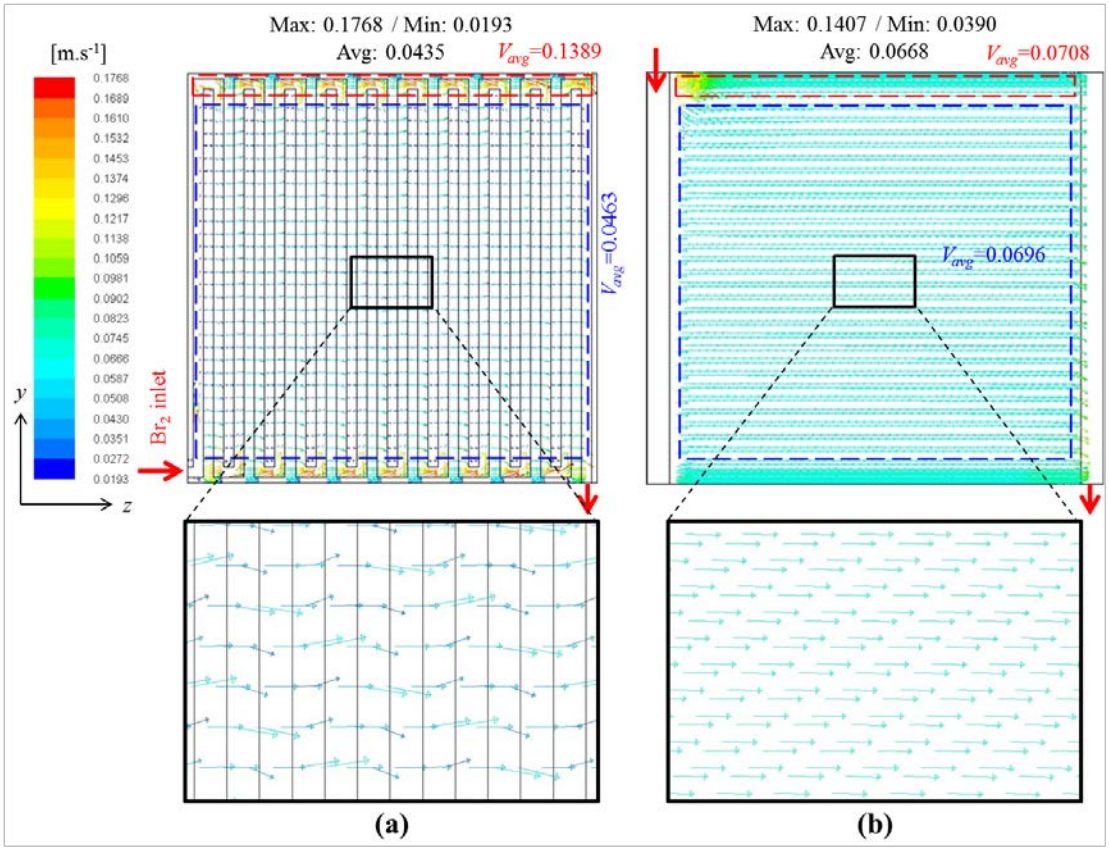

Fig. 6. Velocity profiles over the middle plane of bPM during discharge at 0.9A/cm^2.

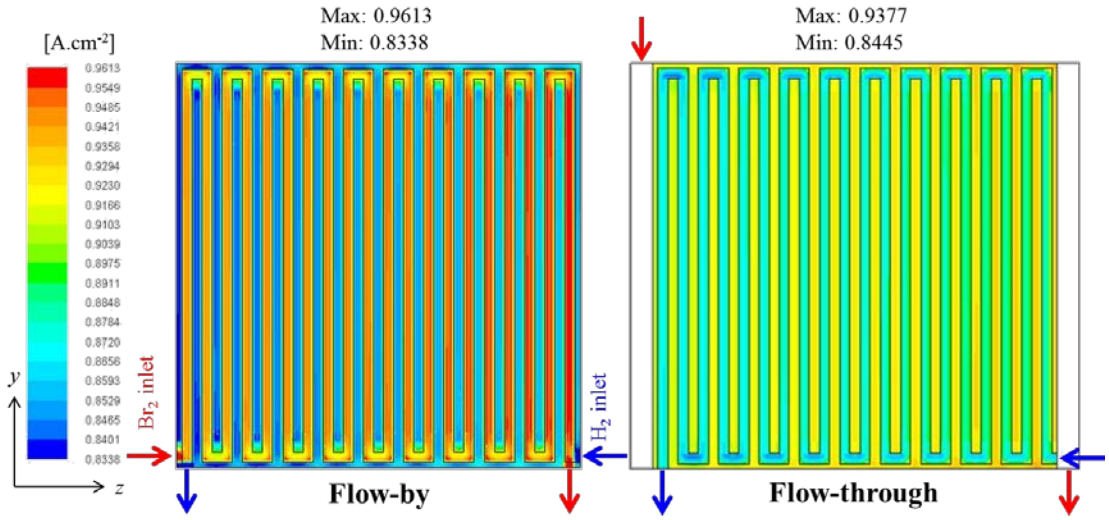

(a)

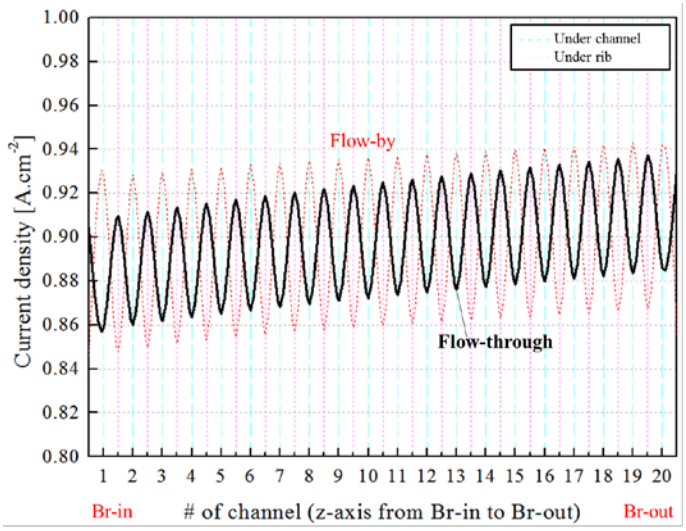

(b)

Fig. 7. (a) Current density distributions over the membrane during discharge at 0.9A/cm^2 and (b) current density variations along the in-plane (z) direction.

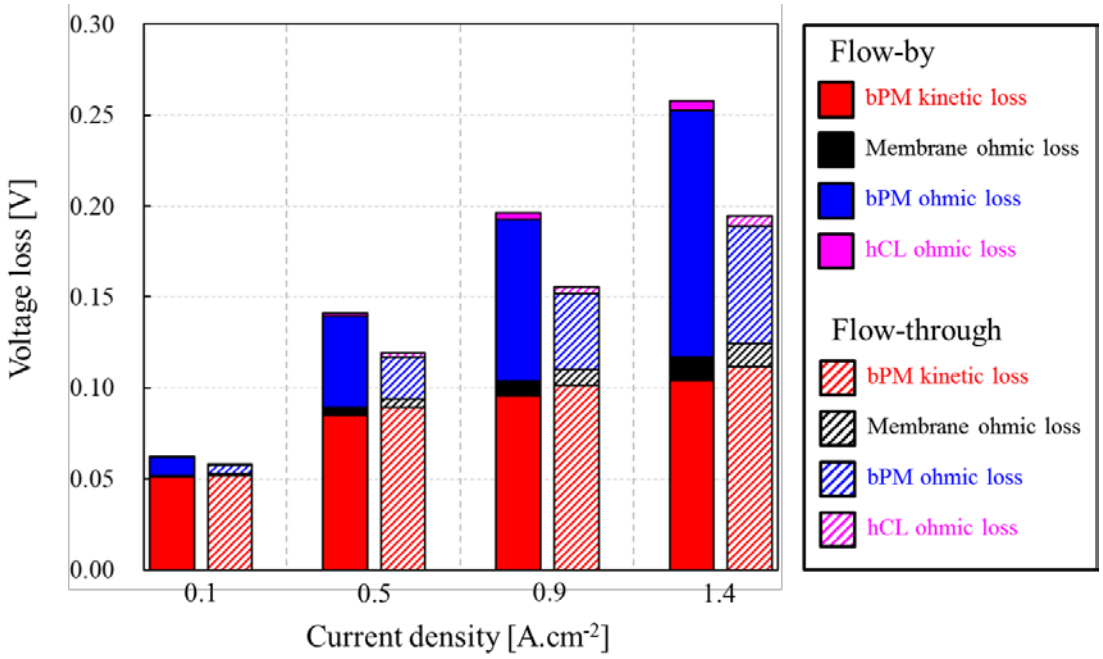

Fig. 8. Individual voltage losses during discharge at 0.9A/cm^2 for the flow-by mode (solid) and flow-through mode (slashed).

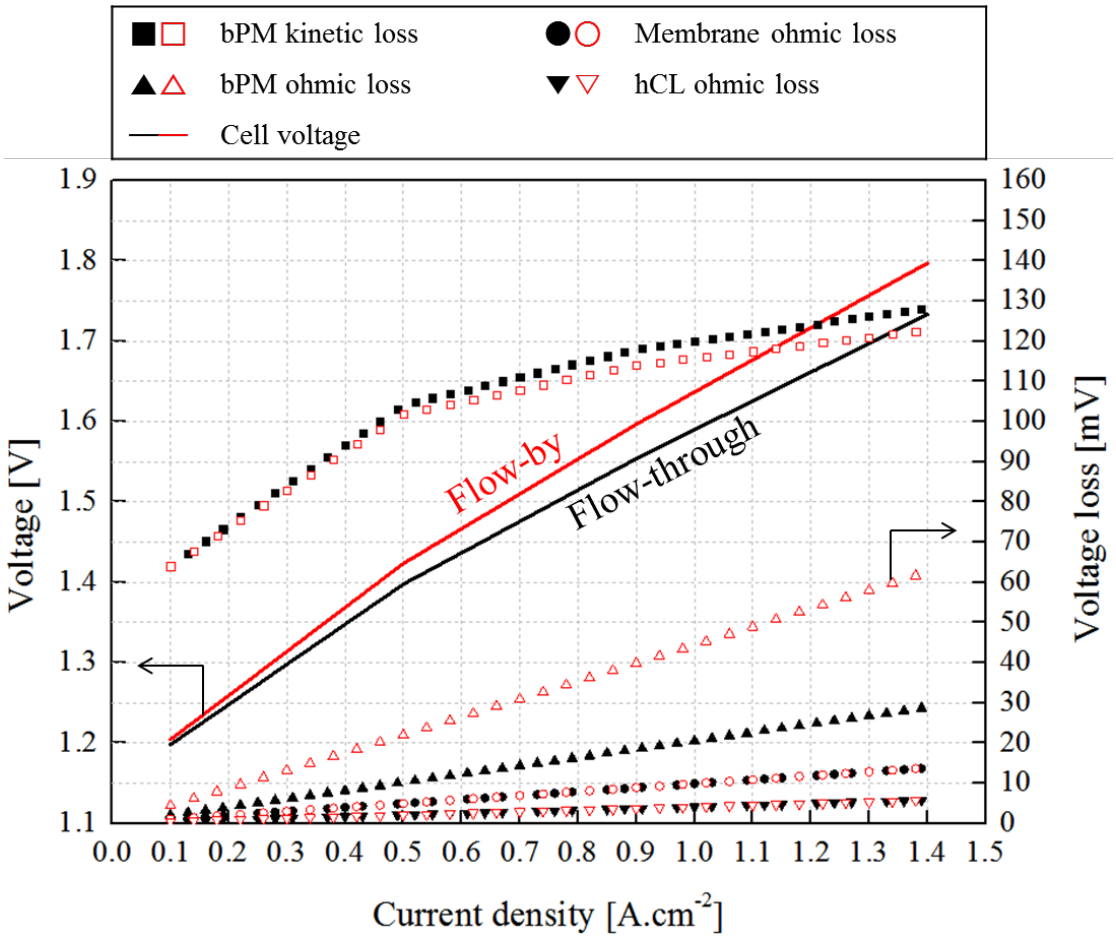

Fig. 9. Polarization curves and voltage losses during charge for the flow-by mode (red line or empty symbols) and flow-through mode (black line or filled symbols).

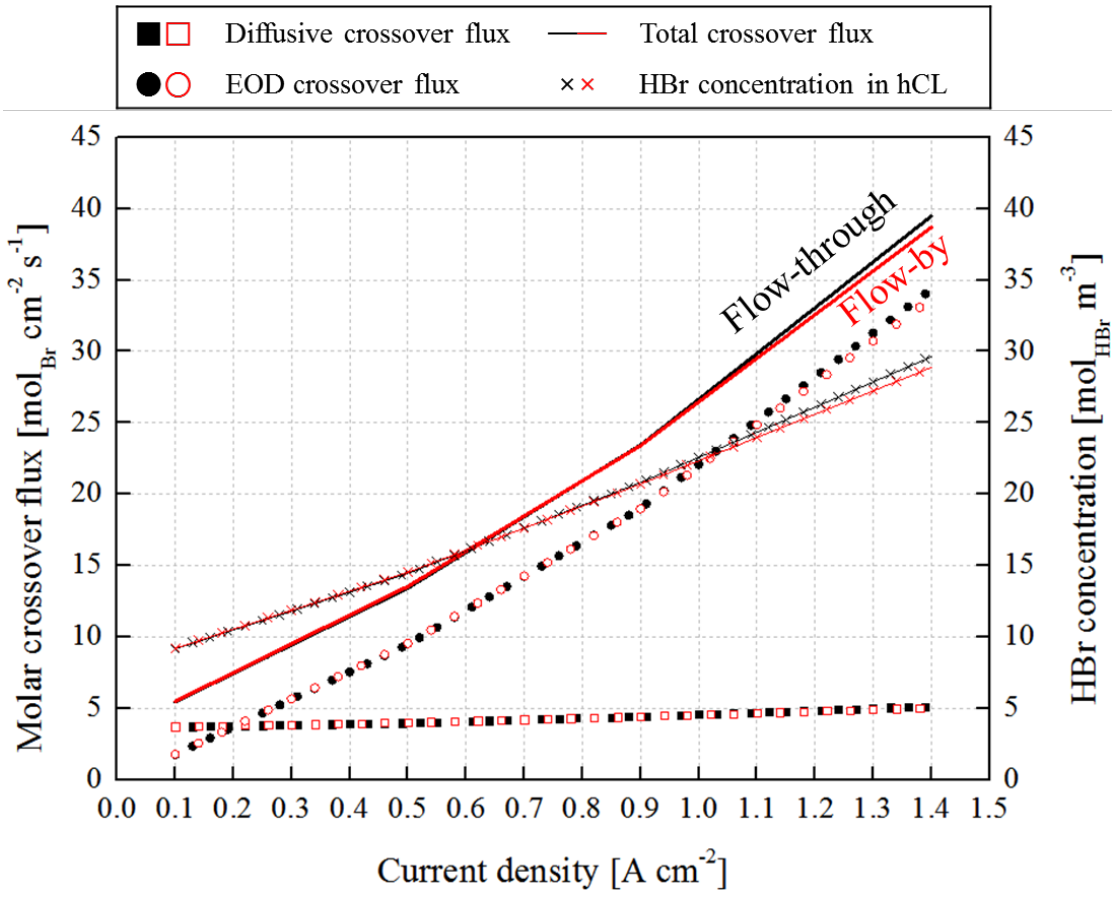

Fig. 10. Effect of flow mode on the crossover fluxes of bromine species during charge.